plasma

MDPI

Article

Study on the Key Influence Factors of Interrupting Characteristics of C_4F_7N Gas Mixture Self-Blast Circuit Breaker

Ke Wang [1], Yuying Shi [2], Bochen Li [2], Yiheng Zhang [2,*], Suoyun Yang [3] and Xianping Zhao [1]

[1] Electric Power Science Research Institute, Yunnan Power Grid Co., Ltd., Kunming 650217, China; wke0410@163.com (K.W.); zxpmy444@163.com (X.Z.)
[2] State Key Laboratory of Electrical Insulation and Power Equipment, Xi'an Jiaotong University, Xi'an 710049, China; shiyy@stu.xjtu.edu.cn (Y.S.); libochen@stu.xjtu.edu.cn (B.L.)
[3] Kunming Power Supply Bureau of Yunnan Power Grid Co., Ltd., Kunming 650299, China; yangsy@snapmail.cc
* Correspondence: 1273964569@stu.xjtu.edu.cn

Abstract

High-voltage self-blast circuit breakers feature complex gas flow field dynamics during the arc interruption process due to the multiple gas chambers and valves in the interrupter. The structure of key interrupter components and the characteristics of the operating mechanism significantly influence the gas flow field behavior, thereby affecting the breaking performance. The C_4F_7N gas mixture is currently the most promising alternative to SF_6. However, the influence mechanisms of various factors on its breaking performance remain unclear, which limits the design of C_4F_7N-based self-blast interrupter chambers. This paper investigates the impact of nozzle throat length and mechanism stroke on the breaking performance of a 126 kV double-motion self-blast circuit breaker prototype by establishing a magnetohydrodynamic (MHD) arc model for C_4F_7N gas mixtures. The results indicate that a longer throat length can enhance the pressure-buildup capability in the expansion chamber to some extent, but its effect on short arcing times is limited, whereas it has a more pronounced influence on medium and long arcing times. However, it also impedes arc energy dissipation, potentially reducing the breaking capability for short and medium arcing times while improving performance for long arcing times. A larger mechanism stroke not only ensures a greater contact gap at current zero for long arcing times but also accelerates the gas flow velocity between the contacts, facilitating arc energy dissipation and enhancing the thermal interruption performance.

Keywords: C_4F_7N gas mixture; self-blast circuit breaker; interruption performance; MHD simulation

Check for updates

Academic Editor: Andrey Starikovskiy

Received: 8 April 2026
Revised: 17 May 2026
Accepted: 18 May 2026
Published: 20 May 2026

Copyright: © 2026 by the authors. Licensee MDPI, Basel, Switzerland. This article is an open access article distributed under the terms and conditions of the Creative Commons Attribution (CC BY) license.

1. Introduction

In the power industry, SF_6 gas has long been widely utilized in high-voltage switchgear due to its exceptional arc-quenching capability, insulation properties, and chemical stability [1]. However, SF_6 possesses an extremely high global warming potential (GWP), which is 23,500 times that of CO_2, and can persist in the atmosphere for up to 3200 years [2]. With the intensification of global climate change issues and increasingly stringent environmental regulations, the search for environmentally friendly alternatives to SF_6 gas has become crucial [3]. Currently, synthetic C_4F_7N gas represents the most promising candidate, exhibiting approximately double the dielectric strength of SF_6 while maintaining a global warming potential (GWP) of about 2100 CO_2-equivalent [4]. Due to its relatively

high boiling point, it requires mixing with buffer gases such as CO_2 or N_2 for practical application [5,6]. Meanwhile, as the voltage levels in power systems continue to increase, the demand for high-capacity interrupting capability has hindered the broader adoption of eco-friendly gas circuit breakers, making research on high-voltage-level environmentally friendly circuit breakers an urgent priority.

Currently, some research is being conducted on the interrupting performance of C_4F_7N mixture. GE has conducted tests on a 420 kV disconnect switch and a 145 kV high-voltage gas circuit breaker, preliminarily confirming that the g3 gas mixture (5% C_4F_7N/95% CO_2) possesses an arc-interrupting performance comparable to SF_6. The g3 mixture exhibits a similar arc quenching performance to a 70% CO_2–30% O_2 mixture, while SF_6's arc-quenching characteristics were significantly superior to both [7,8]. Zhang et al. conducted simulation and experimental studies on a 40.5 kV prototype using a 5% $C_4F_7N/CO_2/O_2$ mixed gas. Results indicate that the axial thermal convection capability of the C_4F_7N mixture is stronger than that of SF_6 gas, and increasing the O_2 proportion in the mixture enhances arc energy dissipation [9,10]. Lin Shen et al. compared the switching performance of C_4F_7N/CO_2 mixed gases with SF_6 at different gas ratios. SF_6 gas arcs exhibit higher arc core temperatures and smaller arc radii. Increasing the C_4F_7N proportion in the mixed gas raises the arc core temperature and reduces the arc radius [11]. Current research indicates that C_4F_7N mixed gases exhibit excellent interrupting capabilities. However, the mechanisms underlying the factors influencing the interrupting performance of C_4F_7N mixed gases remain unclear, limiting their design and performance optimization.

In previous work, we presented a detailed comparison of the arc characteristics between SF_6 gas and C_4F_7N mixture, revealing that SF_6 under pressure within the arc-extinguishing chamber exhibits rapid accumulation and dissipation compared to C_4F_7N mixed gas [12]. Therefore, achieving a comparable interrupting performance solely by replacing the gas in existing SF_6 arc-extinguishing chambers is unfeasible. For high-capacity environmentally friendly gas circuit breakers, understanding the influence mechanism of C_4F_7N mixed-gas self-blast arc-extinguishing chamber design parameters on interrupting performance is crucial for structural optimization of the arc-extinguishing chamber. This knowledge holds significant importance for the development of high voltage self-blast circuit breakers.

This paper focuses on a 126 kV/40 kA C_4F_7N double-action self-blast circuit breaker. It investigates the nozzle throat length of arc-extinguishing chamber and the mechanism travel of its motion characteristics—two critical design parameters. By comparing the interrupting characteristics of the arc-extinguishing chamber under different parameters, this study investigates the influence mechanisms of various factors on interrupting performance. It provides theoretical guidance for analyzing the interrupting characteristics of environmentally friendly gas circuit breakers and optimizing the design of arc-extinguishing chambers.

2. Arc Simulation Model

2.1. Geometric Model Configuration and Breaking Mechanism

Figure 1 shows a simplified two-dimensional axisymmetric simulation geometry of the arc-extinguishing chamber for a 126 kV/40 kA self-blast circuit breaker. The upper and lower sections respectively depict the two states of the circuit breaker: closing and opening. The moving components of the arc-extinguishing chamber initiate movement from the closed state until reaching the open state. Specifically, the stationary arc contact moves toward the left side of the illustration, while the shielding cover, moving main contact, moving arc contact, and expansion chamber move toward the right, compressing the volume within the compression chamber.

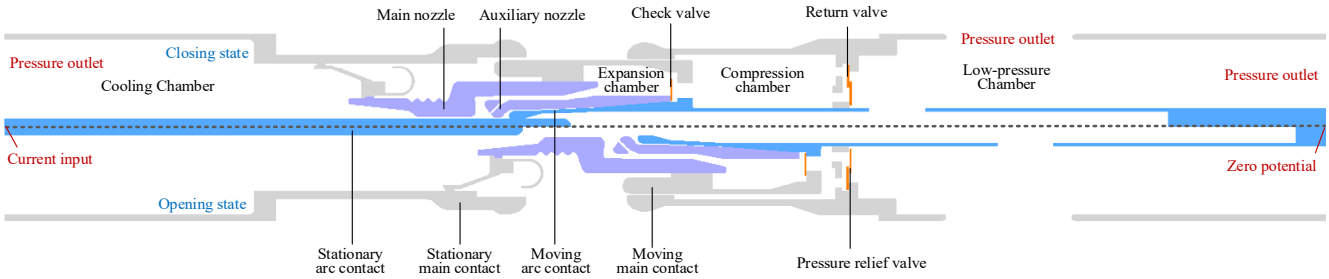


Figure 1. Simulation schematic representation of a 126 kV/40 kA self-blast circuit breaker geometry.

When interrupting high currents, an arc forms between the contacts after separation. As the arc contacts gap increases, the stationary arc contact gradually withdraws from the nozzle. The gas-blow effect generated by high-pressure gas from the expansion chamber then acts upon the arc. During high short-circuit currents, the intense arc erosion of the nozzle generates PTFE vapor. This vapor flows back with the hot gas into the expansion chamber, increasing pressure. When the pressure on the expansion chamber side of the check valve exceeds that on the compression chamber side, the check valve moves toward the compression chamber side and closes. The gas pressure within the compression chamber continues to rise. When the force acting on the relief valve exceeds the pre-compression force of the spring on its right side, the relief valve will be driven to move rightward, discharging the gas from the compression chamber to the right as shown. The gas flow generated by the high-pressure gas in the expansion chamber flows along the arc through the nozzle, extinguishing the arc when the current crosses zero.

The arc-quenching chamber contains a mixed gas with a composition of 5% C_4F_7N, 81% CO_2, and 14% O_2, at a relative gas pressure of 0.7 MPa and an initial temperature of 300 K. In the simulation, the potential of the moving main contact and the hollow arc contact is set to zero. The current input point is positioned on the outer side of the stationary arc contact, and a pressure outlet is configured at the indicated location.

2.2. Arc MHD Simulation Model

Based on the two-dimensional axisymmetric geometric model of the self-blast circuit breaker described above, a magnetohydrodynamic (MHD) simulation model was established using the ANSYS Fluent platform (version 12.1) to characterize the thermal plasma behavior during the arc-extinction process in the arc-extinguishing chamber. The governing equations were solved using the finite volume method, with customized User-Defined Functions (UDFs) to couple the electromagnetic source terms and the physical properties of the C_4F_7N gas mixture. The arc is treated as a thermal plasma, disregarding the influence of the thin sheath layer near the electrodes. It is assumed that the arc plasma is quasi-electrically neutral and maintains local chemical and thermodynamic equilibrium. The flow field is described using the modified Navier–Stokes equations, whose standard form is shown in Equation (1):

$$\frac{\partial(\rho\varphi)}{\partial t} + \nabla \cdot (\rho\varphi \boldsymbol{V}) - \nabla \cdot (\Gamma \nabla\varphi) = S_\varphi \quad (1)$$

In the equation, ρ is the gas density; φ is the physical quantity to be determined; t is time; V is the velocity vector; Γ is the diffusion coefficient; and S_φ is the source term. Equation (1) represents a comprehensive expression of the conservation equations for mass, momentum, and energy, as well as the mass concentration equation for ablation vapor. The specific forms of each term are shown in Reference [13].

In the momentum conservation equation, the magnetic field's azimuthal component B_θ is solved using Biot–Savart's law, while the electric field strength E in the energy conservation equation is determined via the continuity equation for the current. The respective calculation formulas are shown in Equations (2) and (3):

$$\frac{1}{r}\frac{\partial}{\partial r}(rB_\theta) = \mu_0 J_z, \tag{2}$$

$$\nabla \cdot (\sigma \nabla \Phi) = 0, \tag{3}$$

in which μ_0 is the magnetic permeability of free space and r is the arc radius.

Arc energy dissipation primarily occurs through three mechanisms: conduction, convection, and radiation. Conduction and convection are already accounted for in the conservation equations of the gas flow field, while radiation is solved by introducing a source term, q, into the energy conservation equation. In this paper, the net emission coefficient method (NEC) is employed to model the radiation behavior of the arc [14]. During the interruption of short-circuit currents, turbulent effects emerge in the gas flow field within the arc-extinguishing chamber. Turbulence strongly affects the arc-plasma evolution and the associated energy-dissipation mechanisms. The k–ε turbulence model is commonly used in fluid dynamics to describe the dynamics and thermodynamics of fluids under turbulent flow conditions. Previous studies have demonstrated its applicability in arc simulation calculations. For C_4F_7N mixed gases, this study employs the standard k–ε turbulence model to characterize the turbulent flow behavior and adjusts the constants in the equations to ensure simulation accuracy.

During the burning of the arc, the expansion of the arc radius causes ablation of the PTFE material at the nozzle, generating a large amount of PTFE vapor. This PTFE vapor then carries significant arc energy into the expansion chamber, playing a crucial role in establishing the pressure. This study establishes an ablation enthalpy model to describe nozzle ablation. Considering the localized energy concentration characteristics of the nozzle during high-current interruption and the impact of rapid pressure changes on the ablation evaporation enthalpy of PTFE material [15,16], it is proposed that ablation occurs when the nozzle wall temperature reaches 3400 K. The ablation enthalpy represents the energy required to produce one unit mass of ablation products. Based on the arc energy used for nozzle ablation, the mass flux and ablation rate of PTFE vapor can be determined. Neglecting heat conduction effects, the energy used for ablation constitutes a portion of the arc's outward radiated energy.

The ablation rate of the nozzle material and the variation in the source term of the equation caused by ablation vapor are as follows:

$$Q_{rad} = Mh_a, \tag{4}$$

$$H_a = C_v(p, T_b)T_b + 0.5v^2 + p/\rho, \tag{5}$$

in which Q_{rad} represents the radiant heat flux absorbed by the nozzle; h_a denotes the ablation evaporation enthalpy of PTFE; H_a signifies the energy carried by unit mass of PTFE vapor; C_v indicates the specific heat capacity at a constant volume of PTFE; v represents the radial velocity of the vapor; and ρ denotes the density of the mixed gas.

When solving control equations, gas physical properties are required. These parameters—including density, enthalpy, factors, thermal conductivity, and electrical conductivity—represent gas characteristics and are expressed as ternary nonlinear functions of temperature, pressure, and composition. Since the nozzle undergoes arc erosion under high currents, generating PTFE vapor, the composition of the mixed-gas changes, significantly affecting the physical properties. The equation of state for the plasma mixtures is implemented based

on the assumption of Local Thermodynamic Equilibrium (LTE). The relationship between pressure, density, and temperature accounts for the effects of molecular dissociation and multi-stage ionization at high temperatures. These thermodynamic properties are integrated into the solver via pre-calculated look-up tables to ensure numerical consistency. This study employs physical property parameters for $C_4F_7N/CO_2/O_2$–PTFE gas mixtures within the temperature range of 300–30,000 K and the pressure range of 0.1–10 MPa.

2.3. Experimental Validation of Simulation Models

The L90 short-line fault test represents one of the most severe short-circuit tests. The 126 kV/40 kA C_4F_7N mixed-gas self-blast circuit breaker prototype described herein underwent an L90 short-line fault research test with a short-circuit current of 36 kA at the Xi'an High Voltage Electrical Apparatus Research Institute. Figure 2 shows the prototype used in the research trial, with the test results presented in Table 1.

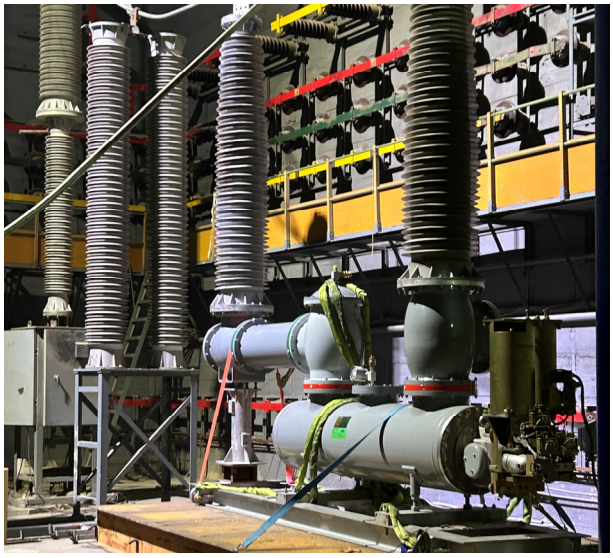


Figure 2. 126 kV/40 kA C_4F_7N mixed-gas circuit breaker L90 research test prototype.

Table 1. L90 short-line fault test results.

Number	Arcing Time	U_{peak}	Results
1	11.8 ms	5421 V	Pass
2	20.2 ms	5401 V	2 half-waves
3	16.0 ms	4905 V	pass

The L90-type test conditions were simulated using the MHD simulation model established in this paper. The arc peak voltages calculated for the following arc durations were: 3445 V for 11.8 ms, 4207 V for 16 ms, and 3015 V for 20.2 ms. During actual testing, the erosive growth of the breaker nozzle with an increasing number of interruptions degrades its interrupting capability. Following the test sequence, the interrupting capacity of the medium-duration arc decreased significantly. Consequently, the calculated arc-extinction peak values were lower than the experimental measurements. Figure 3 compares the simulated arc voltage with the experimentally measured arc voltage under the 20.2 ms long-duration arc condition. The simulation and experimental arc voltage trends exhibit high consistency. Overall, while the simulated arc-extinction peak is lower than the experimental value, the consistent trend partially validates the accuracy of the established model.

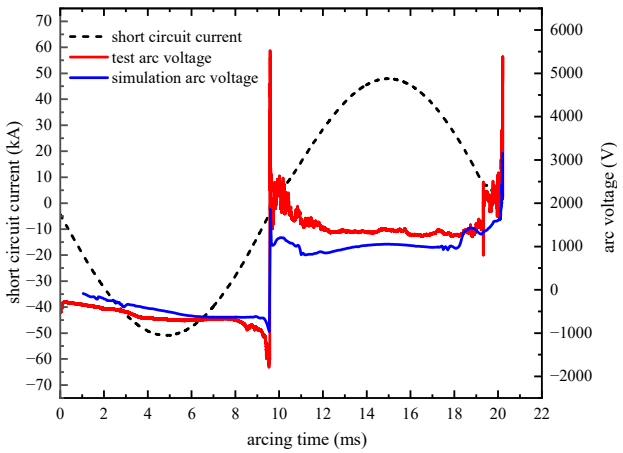


Figure 3. 20.2 ms arcing voltage comparison of L90 short-line fault test and Simulation.

Figure 4 shows the simulation temperature and pressure distribution maps within the arc-extinguishing chamber at different times during 20.2 ms long-arc conditions. The left panel displays the temperature map, while the right panel presents the pressure map.

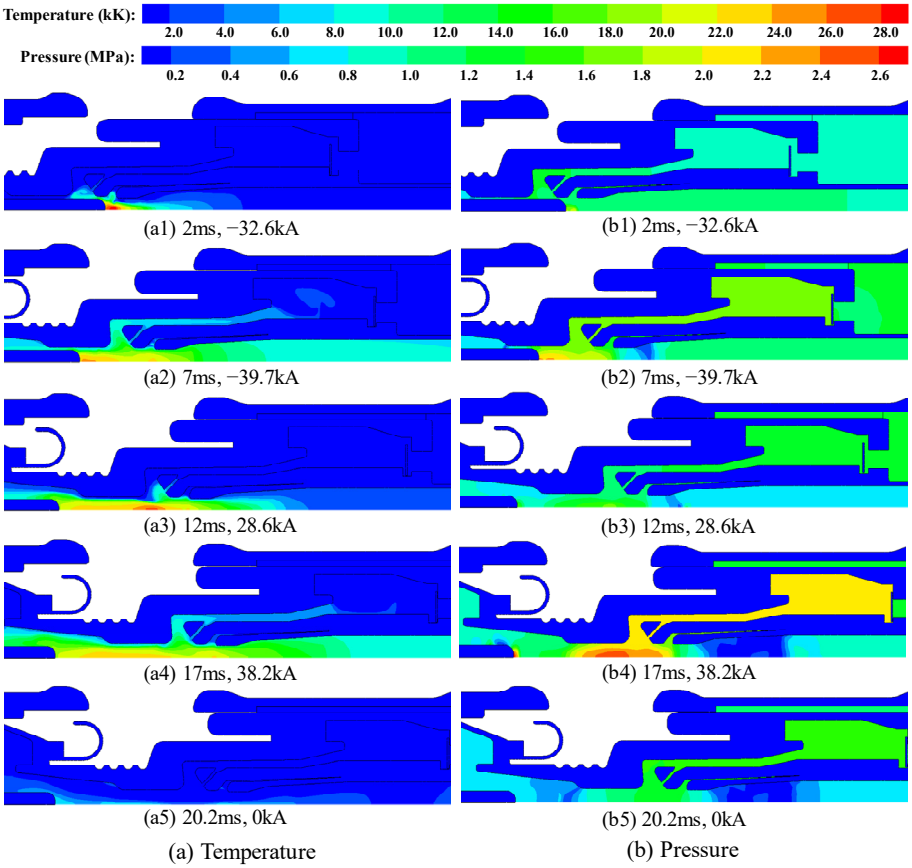


Figure 4. Contour plots of temperature and pressure distribution at 20.2 ms in an arcing simulation.

At 2 ms arcing time, the short-circuit current reaches −32.6 kA. Following the injected energy from the current, the arc burns intensely, with the arc core temperature soaring to 29.1 kK. At this point, the stationary arc contact still blocks the nozzle, causing the arc to diffuse axially and spread longitudinally toward the nozzle. The arc-heated gas has not yet entered the expansion chamber where the average pressure is 0.95 MPa. This pressure is generated by the mechanism compressing the gas within the compression chamber, thus keeping the check valve fully open.

At arcing 7 ms, the short-circuit current reaches −39.7 kA after the peak. The arc burns intensely, with the arc core temperature reaching 24.5 kK. At this point, the stationary arc contact moves to the midpoint of the throat, fully opening the nozzle. Arc-heated gas fills the nozzle area and the interior of the hollow contact, diffusing downstream of the nozzle. The arc-heated gas, carrying PTFE vapor generated by nozzle ablation, continuously expands and flows back upstream through the nozzle channel into the expansion chamber. Consequently, the arc core temperature decreases while the average pressure in the expansion chamber rises to 1.60 MPa. The pressure differential between the two gas chambers causes the check valve to close. At the inlet of the hollow contact and the throat outlet, shock waves form due to the accelerated gas flow velocity.

At 12 ms, with the current increasing to 28.6 kA after zero. The arc core temperature reaches 26.6 kK, causing the arc to contract and eliminating the hot gas backflow phenomenon. At this point, the stationary arc contact has retracted a certain distance from the throat, allowing the arc's hot gases to diffuse downstream toward the nozzle. As the hot gas is expelled, the average pressure in the expansion chamber drops to 1.30 MPa, causing the check valve to open. With the weakening of the gas-blowing, the shock wave phenomenon at the inlet of the transparent contact diminishes.

At 17 ms, the current declines to 38.2 kA after peaking. The arc core temperature dropped to 23.1 kK, causing the arc to burn intensely and expand. At this point, the stationary arc contact has retracted significantly from the throat. Hot gases fill the hollow contact and the downstream region of the nozzle, then flow back into the expansion chamber. The average pressure in the expansion chamber rises to 2.08 MPa, causing the check valve to close. The nozzle now exhibits a strong gas-blowing effect, with shock wave phenomena becoming more pronounced.

At 20.2 ms, the current crosses zero. The arc extinguishes under intense gas-blowing at the nozzle, generating a strong shock wave at the transparent contact inlet and throat outlet. At this point, the expansion chamber retains an average pressure reserve of 1.44 MPa and the check valve remains closed, indicating that the arc-extinguishing chamber possesses a good thermal interrupting capability at zero-crossing.

3. Simulation Analysis of Different Interrupting Performance Factors

3.1. Nozzle Throat Length

In the arc-extinguishing chamber, the design of the nozzle directly influences the pressure and velocity of the gas, thereby affecting the arc-blowing effect. As a critical design factor of the nozzle, the throat length, in conjunction with the mechanical movement characteristics, determines the time required for the stationary arc contacts to withdraw from the nozzle. Based on the arc-extinguishing chamber model shown in Figure 1, this paper examines two throat length configurations: Type A and Type B. Type B extends Type A's throat length by 25%. Using the L90 test current as input, simulations were conducted for three arc-burning durations: 11.8 ms, 16 ms, and 20.2 ms.

Figure 5 shows a comparison of simulation average expansion chamber pressure variations for two throat length structures under three arcing times. For both structures, the 16 ms medium arc duration achieved the highest pressure build-up, followed by the 20.2 ms long arc duration, while the 11.8 ms short arc duration performed the worst. Since the generation of ablation vapor from the nozzle of the self-blast chamber significantly contributes to expansion chamber pressure establishment, the pressure build-up is closely related to both the injected current energy and the dissipation of arc energy. The 11.8 ms arc duration is the shortest, resulting in the lowest current injection energy and thus the poorest pressure build-up effect. Although the 20.2 ms arc injects more energy, its average value is comparable to 11.8 ms, and the contact gap at zero-crossing is larger, yielding

the second-worst pressure build-up. The 16ms arc duration delivers the highest average short-circuit current while maintaining a smaller contact gap at zero-crossing compared to a longer arc, resulting in the strongest pressure-building capability.

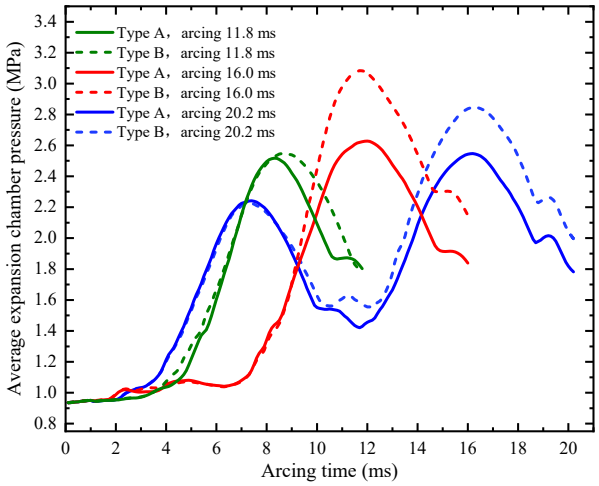


Figure 5. Average pressure variations with arcing time in expansion chambers of different throat lengths.

At an approximate arc of 8 ms, since none of the stationary arc contacts have retracted from the throat, the nozzle exhibits a strong blocking effect on the arc-heated gas. Consequently, under identical operating conditions, the pressure variation trends remain consistent across different throat lengths. Subsequently, the stationary arc contact of Type A first withdraws from the throat, opening the hot gas discharge channel downstream of the nozzle. The pressure-building capacity of its expansion chamber begins to diminish. Due to the longer throat length, the nozzle blocks the arc for a longer duration, allowing hot gases to heat and pressurize the arc-extinguishing chamber more thoroughly. Therefore, compared to Type A, the Type B exhibits enhanced expansion chamber pressure levels across all three arc-burning durations. Specifically, the peak expansion chamber pressures under 11.8 ms, 16ms, and 20.2 ms arcing durations increased by 1.2%, 17.4%, and 11.7%, respectively. The expansion chamber pressures at zero-crossing decreased by 0.1%, increased by 16.8%, and increased by 12.0%, respectively.

For the 11.8 ms arcing time, the current had already passed its peak when the stationary arc contact withdrew from throat structure A. Consequently, the pressure peaks of the two structures differed slightly. Due to the poor pressure-building capability, maintaining the gas blowing intensity near the zero-crossing proved challenging. Thus, the expansion of chamber pressure in Type A experienced stagnation before the zero-crossing, resulting in nearly identical pressures for both structures at the zero-crossing moment. For 16 ms arcing, the nozzles of Type A and Type B open successively before and after the peak, resulting in significant differences in peak pressure and zero-crossing pressure between the two structures. For the 20.2 ms arcing, the nozzle downstream remains closed during the first current half-cycle, resulting in identical initial pressure peaks. Subsequently, Type A opens its nozzle during the pressure decay phase, while throat Type B's nozzle opens in the pressure plateau zone following the first zero-crossing point, where higher pressure levels prevail. During the subsequent pressure-rise phase, the relatively smaller downstream pressure relief channel of structure B causes faster pressure increases in the expansion chamber. As the downstream channel progressively expands, the throat's obstruction effect on hot gas becomes comparable between both structures. In the final pressure release phase, their decline trends converge. Type B exhibits a slightly higher pressure release rate due to its higher peak pressure, indicating a stronger pre-zero gas-blowing effect.

When the current crosses zero, residual hot gases within the arc-extinguishing chamber may cause thermal breakdown between contacts, resulting in failure to interrupt. Therefore, the temperature distribution within the arc-extinguishing chamber at zero-crossing is a critical indicator for determining interrupting ability. Figure 6 shows the temperature distribution along the axis between two arc contacts at the zero-crossing moment under three arcing time conditions for different throat lengths. The origin of the x-axis corresponds to the stationary arc contact end position of the 16 ms and 20.2 ms arc-burning cycles. Table 2 shows the zero-crossing parameters for the six simulation groups. Under the same arc duration, the zero-crossing axis temperature of Type B structure is consistently higher than that of Type A. A longer throat length enhances the obstruction effect on the arc-heated gas, generating higher pressure within the expansion chamber. However, it also reduces the energy-dissipation capacity, resulting in a higher temperature within the arc-quenching chamber during zero-crossing. After extending the throat length, the voltage peaks corresponding to the 11.8 ms and 16 ms operating conditions decreased, while the arc-quenching peak under the 20.2 ms condition increased. Extending the throat length is disadvantageous for arc energy dissipation in the 11.8 ms and 16 ms operating conditions, where the zero-crossing contact gap is smaller, somewhat weakening the thermal breaking capability. However, for the 20.2 ms arc-burning condition with a larger zero-crossing contact gap, the impact is minimal. A longer throat can establish higher pressure, generating stronger gas-blowing effects at zero-crossing and enhancing arc-extinguishing performance.

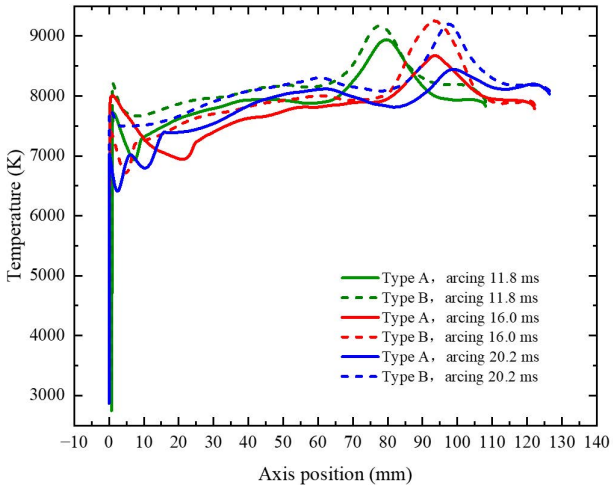


Figure 6. Axial temperature distribution between arc contacts during current zero-crossing in structures with varying throat lengths.

Table 2. Current zero-crossing simulation parameters in structures in different throat lengths.

Arcing Time (ms)	**11.8**		**16.0**		**20.2**	
Throat Length	**A**	**B**	**A**	**B**	**A**	**B**
Average temperature (K)	7931	8178	7783	7935	7817	8130
Voltage peak (V)	3445	3191	4207	3913	3015	3656

3.2. Mechanism Travel

To design the arc-extinguishing chamber for self-blast circuit breakers, the time when the stationary arc contacts are just withdrawn from the throat typically corresponds to the shortest arc duration that can be interrupted. Meanwhile, the contact gap between the contacts relates to the interrupting state associated with a longer arc duration. Generally, a larger opening distance can effectively elongate the arc, facilitating current interruption. Based on the model shown in Figure 1, considering the variation in contact withdrawal time

across different throat lengths, comparative simulations were conducted for a 20.2 ms long arc at various contact gaps for throat lengths A and B. The simulated current conditions were consistent with those in the L90 tests. Due to the larger opening distance for simulation, the simulated model extends the compression chamber by 23 mm based on the structure shown in Figure 1. The mechanism travel of the stationary arc contact remains unchanged, while the mechanism travel of the moving arc contact is shown in Figure 7.

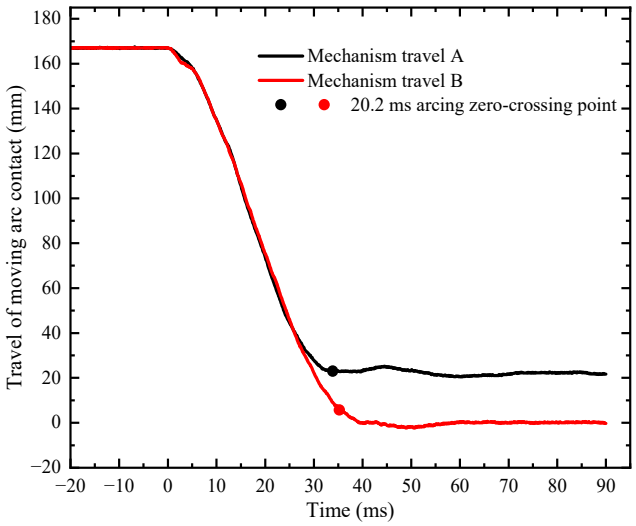


Figure 7. Mechanism travel characteristic curve.

Under essentially the same mechanism speeds, the arc contact Mechanism travel B is extended by 22 mm compared to Mechanism travel A. The diagram indicates the mechanism travels at the zero-crossing point of the current corresponding to a 20.2 ms arc-striking time. For travel A, the mechanism has nearly reached its maximum opening distance at the zero-crossing point of the 20.2 ms arc-striking time, with no remaining speed. For travel B, the mechanism has not yet reached its maximum opening distance at this point and still maintains a relatively high mechanism speed of 2.08 m/s. Compared to travel A, the opening distance of travel B is extended by 16.3 mm at this point.

Figure 8 shows the variation in average pressure in the expansion chamber over arcing time during by simulation. Within the first half-cycle of the current, since the stationary arc contact has not yet retracted from the nozzle, the throat length has minimal impact on pressure establishment in the expansion chamber. Under same mechanism characteristics, expansion chamber pressure establishment exhibits highly consistent results across different throat lengths. In all four simulation sets, the check valves closed approximately 5 ms after arc ignition and remained closed thereafter. Since the nozzle had not yet opened at this point, gas compression within the compression chamber significantly influenced pressure buildup. Consequently, the pressure-building effects varied considerably depending on the specific mechanism characteristics. During the decay following the first pressure peak, the stationary arc contacts sequentially retract from the throat. In the Type A and travel A simulations, the contact retracts from the throat at an arc of 8.5 ms. As the nozzle channel opens, gas discharge through the nozzle accelerates, resulting in a faster rate of decrease in the expansion chamber's average pressure compared to the Type B and travel A simulation. Subsequently, the Type B and travel A simulation pulled out the throat channel at 10.4 ms during the arc ignition phase. The stationary arc contacts for Type A and travel B, as well as Type B and travel B, pulled out the throat channel at 9.2 ms and 10.8 ms, respectively. Within the second current half-cycle, as the nozzle was no longer blocked, the expansion chamber pressures across different throat lengths began to exhibit significant variation,

while pressures with distinct characteristics tended toward consistency. At this point, the check valve had already closed. Pressure buildup in the expansion chamber was no longer related to gas compression in the compression chamber; it primarily stemmed from the heating effect of PTFE vapor generated by ablation, which is carried by the returning hot gas and heats the gas within the expansion chamber. For Type B structures, travel A exhibits a 9.5% increase in peak pressure increment compared to travel B, while the zero-crossing pressure increment decreases by 5.8%. For structures with throat length A, travel A shows a 1.5% reduction in peak pressure increment relative to travel B, with the zero-crossing pressure increment also decreasing by 1.5%. Since the nozzle has already opened at the end of the 20.2 ms arcing, the opening distance of the mechanism has a relatively minor impact on pressure buildup within the arc-extinguishing chamber. For the nozzle, a longer throat not only extends the nozzle withdrawal time but also provides a stronger pressure-blocking ability against downstream pressure release after the stationary arc contact withdraws from the throat. Consequently, higher pressure is established within the arc-extinguishing chamber.

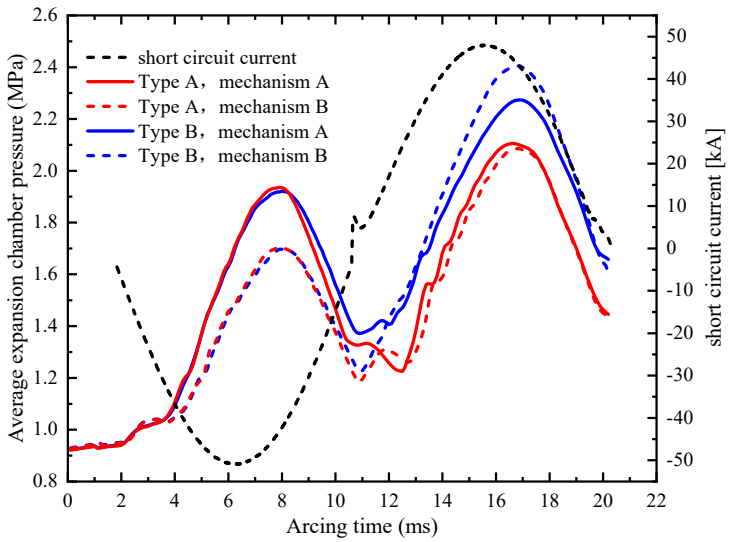


Figure 8. Average pressure variation curves in expansion chambers with varying mechanism characteristics.

Figure 9 shows the temperature distribution along the center axis between the four simulated arc contacts at the zero-crossing moment. Table 3 presents the average axis temperature between contacts and the simulated arc-quenching peak at the zero-crossing moment. Compared to travel A, travel B exhibits lower overall temperatures and a higher arc-quenching peak, indicating that travel B possesses stronger gas thermal dissipation capabilities and relatively superior interrupting performance.

Table 3. Zero-crossing parameters simulation under different mechanism characteristics.

Mechanism Travel	**A**		**B**	
Throat Length	**A**	**B**	**A**	**B**
Average temperature (K)	7833	8028	7820	7756
Voltage peak (V)	3312	3019	3528	4400

Figure 10 shows the gas velocity distribution among the four simulated arc contacts at the zero-crossing moment. The origin of the X-axis is the position of the stationary arc contact end in the travel B. The gas velocity near the stationary arc contact is significantly higher in the travel B simulation compared to the travel A simulation. The arc-extinguishing

chamber of a high-voltage gas circuit breaker relies on generating a strong gas-blowing effect on the arc at zero-crossing to dissipate its energy. At zero-crossing, travel B maintains a certain velocity, whereas travel A has no velocity. A certain mechanism velocity at zero-crossing helps increase the gas flow velocity in the arc zone, thereby enhancing arc energy dissipation and improving thermal arc interrupting performance.

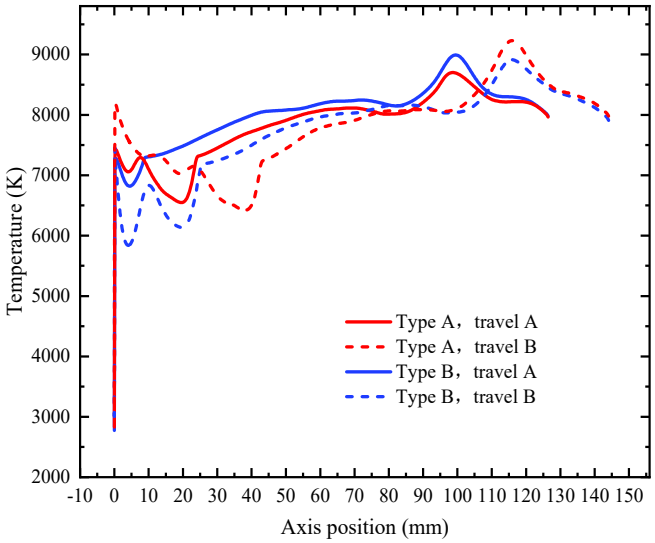


Figure 9. Temperature distribution along the central axis between contacts with different mechanism characteristics at zero-crossing.

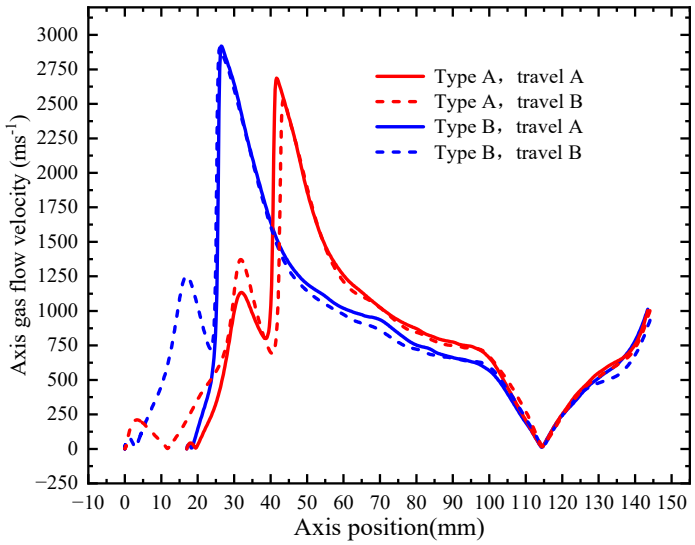


Figure 10. Gas flow velocity distribution along the central axis between contacts at zero-crossing.

4. Discussion and Conclusions

This study presents simulation calculations of the key factors affecting the interrupting performance of the arc-extinguishing chamber and operating mechanism in C_4F_7N mixed-gas circuit breakers. Based on a 126 kV/40 kA double-action self-blast prototype circuit breaker, an arc MHD model accounting for nozzle ablation effects was established. Simulations were conducted under L90 short-line fault test conditions, yielding results consistent with experimental data. Subsequently, simulations were performed for varying parameters of two critical design elements: nozzle throat length and operating mechanism stroke. The conclusions are as follows.

Extending the throat length enhances the nozzle's gas blocking effect, thereby improving the expansion chamber's pressure building capacity to some extent. However, this also hinders arc energy dissipation, leading to increased temperatures at the zero-crossing contacts. For short arcing, the zero-crossing point often occurs near the moment the contact is withdrawn from the throat. Therefore, throat length has a minor impact on expansion chamber pressure build-up but significantly affects arc energy dissipation. Increasing the throat length reduces the arc voltage peak but weakens thermal breaking performance. Medium arcing, characterized by higher average currents and intense combustion, are significantly affected by throat length in pressure build-up. Although the arc voltage peak decreases, it remains at a relatively high level. For long arcing, the throat is already sufficiently open at zero-crossing, resulting in a slightly lower impact on pressure build-up compared to medium arcs. The higher pressure level established helps maintain gas-blowing intensity during the zero-crossing phase of long arcing, thereby enhancing interrupting performance and increasing the arc voltage peak. Given the superior interrupting performance of medium-duration arcs, when designing the nozzle of the arc-extinguishing chamber, the throat length should be extended as much as possible to enhance the interrupting performance of long-duration arcs, while ensuring the performance of short-duration arcs.

The design of the mechanism travel is closely related to the breaking performance of long arcing. A longer mechanism stroke ensures that when the long arc crosses zero, not only is a larger contact gap maintained, but a certain mechanism speed is also preserved. This enhances the flow velocity of the arc-quenching gas, increases the energy-dissipation intensity of the arc-heated gas, lowers the temperature in the arc core region at zero-crossing, and improves the thermal breaking performance of the arc-quenching chamber. However, a larger contact gap requires greater operating force from the mechanism. Therefore, during the design process the mechanism stroke should be maximized as much as possible within the constraints of the compression cylinder length and the mechanism's operating force.

For future research in this direction, several aspects warrant further investigation. First, a three-dimensional (3D) magneto-hydrodynamic (MHD) simulation should be developed to capture the non-axisymmetric arc root movement and distortion under high-current conditions. Second, the long-term chemical degradation and dielectric recovery characteristics of the C_4F_7N/CO_2 mixture after multiple arc interruptions need to be systematically quantified through experimental coupling. These studies will provide more comprehensive guidelines for the optimization of eco-friendly high-voltage circuit breakers.

Author Contributions: Conceptualization, K.W., Y.S. and X.Z.; methodology, Y.S.; software, Y.S., B.L. and Y.Z.; validation, Y.S., B.L. and Y.Z.; formal analysis, Y.S.; data curation, Y.S., B.L. and Y.Z.; writing—original draft preparation, Y.S.; writing—review and editing, Y.S., B.L. and Y.Z.; project administration, K.W., S.Y. and X.Z. All authors have read and agreed to the published version of the manuscript.

Funding: This research was funded by The Science and Technology Project of China Southern Power Grid, grant number YNKJXM20240022.

Data Availability Statement: The original contributions presented in this study are included in the article. Further inquiries can be directed to the corresponding author.

Conflicts of Interest: Authors Ke Wang and Xianping Zhao were employed by the company Yunnan Power Grid Co., Ltd., Author Suoyun Yang was employed by the company Kunming Power Supply Bureau of Yunnan Power Grid Co., Ltd. The remaining authors declare that the research was conducted in the absence of any commercial or financial relationships that could be construed as a potential conflict of interest. The funders had no role in the design of the study; in the collection, analyses, or interpretation of data; in the writing of the manuscript; or in the decision to publish the results.

References

1. Li, X.; Zhao, H.; Murphy, A.B. SF_6 -Alternative Gases for Application in Gas-Insulated Switchgear. *J. Phys. D Appl. Phys.* **2018**, *51*, 153001. [CrossRef]
2. Masson-Delmotte, V.; Zhai, P.; Pirani, A.; Connors, S.L.; Péan, C.; Berger, S.; Caud, N.; Chen, Y.; Goldfarb, L.; Gomis, M.I.; et al. Climate change 2021: The physical science basis. In *Contribution of Working Group I to the Sixth Assessment Report of the Intergovernmental Panel on Climate Change*; Cambridge University Press: Cambridge, UK, 2021; Volume 2, p. 2391.
3. Rabie, M.; Franck, C.M. Assessment of Eco-Friendly Gases for Electrical Insulation to Replace the Most Potent Industrial Greenhouse Gas SF_6. *Environ. Sci. Technol.* **2018**, *2*, 369–380. [CrossRef] [PubMed]
4. Zhang, B.; Zhou, R.; Wang, K.; Guo, Z.; Li, X.; Cao, M.; Deng, J.; Wang, D. Arc Interruption Performance of C_4F_7N-CO_2 Mixture in a 126 kV Disconnector. *IEEE Trans. Power Deliv.* **2022**, *38*, 1197–1207. [CrossRef]
5. Guo, Z.; Li, X.; Li, B.; Fu, M.; Zhuo, R.; Wang, D. Dielectric Properties of C5-PFK Mixtures as a Possible SF6 Substitute for MV Power Equipment. *IEEE Trans. Dielectr. Electr. Insul.* **2019**, *26*, 129–136. [CrossRef]
6. Zhang, B.; Uzelac, N.; Cao, Y. Fluoronitrile/CO_2 Mixture as an Eco-Friendly Alternative to SF_6 for Medium Voltage Switchgears. *IEEE Trans. Dielectr. Electr. Insul.* **2018**, *25*, 1340–1350. [CrossRef]
7. Kieffel, Y.; Biquez, F. SF6 Alternative Development for High Voltage Switchgears. In *2015 IEEE Power & Energy Society General Meeting*; IEEE: New York, NY, USA, 2015; p. 383.
8. Lee, W.-Y.; Jun, J.-U.; Oh, H.-S.; Park, J.-K.; Oh, Y.-H.; Song, K.-D.; Jang, H.-J. Comparison of the Interrupting Capability of Gas Circuit Breaker According to SF_6, g3, and CO_2/O_2 Mixture. *Energies* **2020**, *13*, 6388. [CrossRef]
9. Zhang, B.; Zhou, R.; Hao, M.; Pu, Y.; Li, X.; Jiang, X.; Zhu, K.; Deng, Y. Research on Application of C_4F_7N Gas Mixture in 40.5 kV Circuit Breaker (Part I): Simulation and Evaluation of Arc Extinguishing Performance. *Proc. Chin. Soc. Electr. Eng.* **2022**, *42*, 8750–8762. (In Chinese)
10. Zhang, B.; Zhou, R.; Hao, M.; Yang, T.; Li, X.; Jiang, X.; Zhu, K.; Deng, Y. Research on Application of C_4F_7N Gas Mixture in 40.5 kV Circuit Breaker (Part II): Arc Extinguishing Performance Tests and Decomposition Property. *Proc. Chin. Soc. Electr. Eng.* **2022**, *42*, 9147–9159. (In Chinese)
11. Song, Y.; Lin, X.; Xu, J.; Zhang, J. Interruption Performance of C_4F_7N/CO_2 Gas in High-voltage Circuit Breaker. *High Volt. Eng.* **2023**, *49*, 971–981. (In Chinese)
12. Cao, M.; Wang, G.; Zhang, B.; Shi, Y.; Deng, J.; Li, X. Effect of PTFE Nozzle Ablation Degradation on Pressure Buildup in C_4F_7N Eco-friendly Gas Circuit Breaker. *Proc. CSEE* **2026**, *46*, 3442–3453. (In Chinese)
13. Zhang, B.; Cao, M.; Wang, Z.; Zhou, R.; Deng, J.; Li, X.; Wang, Z.; Wang, P. Dielectric Recovery Characteristics of SF_6 Circuit Breaker under Repeated Lightning Strikes. *Electr. Power Syst. Res.* **2025**, *241*, 111348. [CrossRef]
14. Wu, Y.; Wang, C.; Sun, H.; Murphy, A.; Rong, M.; Yang, F.; Chen, Z.; Niu, C.; Wang, X. Properties of C_4F_7N-CO_2 Thermal Plasmas: Thermodynamic Properties, Transport Coefficients and Emission Coefficients. *J. Phys. D Appl. Phys.* **2018**, *51*, 15. [CrossRef]
15. Park, J.; Ha, M. Experimental and Numerical Studies of Nozzle Ablation and Geometric Change in Real Gas Circuit Breakers. *IEEE Trans. Power Deliv.* **2022**, *37*, 4506–4514. [CrossRef]
16. Gonzalez, J.-J.; Pierre, F.; Reichert, F.; Petchenko, A. PTFE Vapor Contribution to Pressure Changes in High-Voltage Circuit Breakers. *IEEE Trans. Plasma Sci.* **2015**, *43*, 2703–2714. [CrossRef]

Disclaimer/Publisher's Note: The statements, opinions and data contained in all publications are solely those of the individual author(s) and contributor(s) and not of MDPI and/or the editor(s). MDPI and/or the editor(s) disclaim responsibility for any injury to people or property resulting from any ideas, methods, instructions or products referred to in the content.